Numerical Simulation of the Droplet Formation in a Cross-Junction Microchannel Using the Lattice Boltzmann Method

Zilu Li, Jinfen Kang, Jae Hyun Park, Yong Kweon Suh*
Department of Mechanical Engineering, Dong-A University,
840 Hadan-dong, Saha-gu, Busan 604-714, Korea

This study describes the numerical simulation of two-dimensional droplet formation and the following motion by using the Lattice Boltzmann Method (LBM) with the phase field equation. The free energy model is used to treat the interfacial force and the deformation of a binary fluid system, drawn into a cross-junction microchannel. While one fluid is introduced through the central inlet channel, the other fluid is drawn into the main channel through the two vertical inlet channels. Due to the effect of surface tension on the interface between the two fluids, the droplets of the first fluid are formed near the cross-junction. The aim in this investigation is to examine the applicability of LBM to the numerical analysis of the droplet formation and its motion in the microchannel. It was found from comparison with the experimentally visualized patterns that LBM with the free energy model can reproduce the droplet formation successfully. However because of the stability problem which is intrinsic for high surface-tension cases, it requires a very long computational time. This issue is to be resolved in the future.

Key Words : Lattice Boltzmann Method, Cross-Junction Microchannel, Droplet Formation

Nomenclature

c : Reference velocity
E : Error
e : Discrete particle velocity
F : Free-energy function
f_i : Distribution function of the total density
$\tilde{f}_i$: Distribution function of the total density after the collision process
g_i : Distribution function of the density difference
$\tilde{g}_i$: Distribution function of the density difference after the collision process
$P_{\alpha\beta}$: Pressure tensor
Δt : Time step
$\boldsymbol{u}$: Fluid velocity
U_{in} : Maximum velocity at the horizontal inlet
$\tilde{u}_j$: Normalized velocity
u_j : Normalized exact solution
V_{in} : Maximum velocity at the vertical inlet
Δx : Space step

Greek letters

Γ : Mobility coefficient of the fluids
$\Delta\mu$: Chemical potential difference
ξ : Interfacial width
ρ : Total density of both fluids
ρ_a : Density of fluid A
ρ_b : Density of fluid B
ρ_0^* : Reference density (dimensional)
σ : Surface tension at the interface
ν : Kinematic viscosity of both fluids
φ : Density difference between fluid A and B

Superscripts

$*$: Dimensional variable
eq : Equilibrium term

* Corresponding Author,
E-mail : yksuh@dau.ac.kr
TEL : +82-51-200-7648; **FAX** : +82-51-200-7656
Department of Mechanical Engineering, Dong-A University, 840 Hadan-dong, Saha-gu, Busan 604-714, Korea. (Manuscript **Received** August 29, 2006; **Revised** November 30, 2006)

Subscripts

a : Fluid A
b : Fluid B
i : Link number
in : Inlet

1. Introduction

Recently, the Lattice Boltzmann Method (LBM) has rapidly evolved into a self-standing research subject within the theoretical framework of statistical mechanics. It was developed as a spin-off of lattice gas cellular automata and has become the most noticeable discrete kinetic theory (Succi, 2001). LBM is different from the other conventional methods, which are mainly based on discretization of macroscopic continuum equations, i.e., the continuity and Navier-Stokes equations. LBM is resulted from microscopic models and macroscopic kinetic equations. Thereby, it incorporates the essential physics of microscopic and macroscopic process. The averaged properties of the macroscopic fluids, such as density and velocity, are the collective result of many particle behaviors in the lattice system.

During the last decade, LBM has been developed significantly and it is now considered as an alternative and versatile numerical simulation method in computational fluid dynamics. Variety of flow regimes, including unsteady flows, phase separation, evaporation, condensation, cavitations, solute/heat transport, buoyancy and interactions with surfaces have been realized by LBM. The wide applications of LBM arise from the following fundamental advantages (Sukop, 2006):

(1) LBM is free from the pressure equation,
(2) the programming is very simple,
(3) quite suitable for the parallel computation,
(4) the flows involving complex boundaries and interfacial phenomena can be easily treated.

In the present work, the LBM is used as the numerical tool to study the droplet formation and its motion in a cross-junction microchannel. The reason for selecting the microchannel as the application area is due to the fact that droplets have been used by many experimental investigators for chemical reaction of sample fluids in micro-devices. Besides, in micro scales the dominant effect of the surface tension makes the droplet shapes much simpler than in the macro scales, which in turn permits the currently available computer capacity to produce reliable data concerning the droplet behavior.

The free energy model of LBM is employed here, which was first proposed by Orlandini et al.(1995) and Swift et al.(1996). They have used this model to analyze two phase flows in order to implement the interfacial force and to track the interface deformation of a binary fluid system. Simulation of the formation, motion, deformation and breakup of droplets in a channel is a big challenge which can be handled with the free energy model of LBM. Problems of the multiphase fluid motion have been simulated more frequently by the 'color' model and the 'local interaction' model, otherwise called as the 'Shan and Chen' model (Gunstensen et al., 1991 ; Shan and Chen, 1993 ; Orlandini et al., 1995 ; Swift et al., 1996). Free energy model have been employed by very few researchers in the past for solving the problem of the motion of a binary immiscible fluid. The major advantage of this model is the correspondence between variables used for the simulation and the physical quantities, whereas both the color model and local interaction model of LBM lack a clear relation to classical thermodynamics..

The following section describes the LBM and the free energy model in sufficient detail. The computational model description is given in Sec. 3. A computer code is developed based on the free energy model of LBM to analyze the present problem. The numerical stability and accuracy of the present model is elaborated in Sec. 4. The results obtained using the computer code developed is presented in Sec. 5, which is followed by conclusions in Sec. 6.

2. Governing Equations

In this study, a binary fluid is considered with components A and B. Both fluids are assumed to have the same density ρ^* for convenience (e.g., water and oil). The two fluid components are

also assumed to be immiscible in principle. But, for the effective numerical computation slight miscibility should be permitted, especially at the interface between the two components. This means that an infinitesimal fluid blob is thought to be composed of two components with the partial density ρ_a^* and ρ_b^* respectively. The total density is then given by $\rho^*=\rho_a^*+\rho_b^*$ and the density difference $\varphi^*=\rho_a^*-\rho_b^*$ serves as a phase field. The latter is also called the 'order parameter'. These variables are non-dimensionalized by a certain reference density, ρ_0^*. In the incompressible fluid limit, $\varphi=1$ for the case when the fluid is locally composed of the A fluid only, whereas, $\varphi=-1$ for the case of the B fluid only. Two distribution functions $f_i(\boldsymbol{r},t)$ and $g_i(\boldsymbol{r},t)$ are used to describe the population of the dimensionless total density ρ and the dimensionless density difference (respectively) on each of the i links of the two-dimensional D2Q9 lattice shown in Fig. 1 (Suh and Kang, 2006). The evolution of both distribution functions are governed by the single relaxation time Boltzmann equations of BGK type:

$$f_i(\boldsymbol{r}+\boldsymbol{e}_i\Delta t,t+\Delta t)-f_i(\boldsymbol{r},t)=-\frac{1}{\tau_\rho}[f_i(\boldsymbol{r},t)-f_i^{eq}(\boldsymbol{r},t)] \tag{1}$$

$$g_i(\boldsymbol{r}+\boldsymbol{e}_i\Delta t,t+\Delta t)-g_i(\boldsymbol{r},t)=-\frac{1}{\tau_\varphi}[g_i(\boldsymbol{r},t)-g_i^{eq}(\boldsymbol{r},t)] \tag{2}$$

Here τ_ρ and τ_φ are independent relaxation parameters, and $f_i^{eq}(\boldsymbol{r},t)$ and $g_i^{eq}(\boldsymbol{r},t)$ are local equilibrium distribution functions along the link i at the position $\boldsymbol{r}$ and at the time, t. Here all the variables are dimensionless and measured in terms of the lattice units. That is, the spatial coordinates and the physical lengths are scaled by the lattice size Δx^*, the time by the time step Δt^*, the velocities by the reference velocity $c^*=\Delta x^*/\Delta t^*$ and the distribution functions by the reference density ρ_0^*. Accordingly, the dimensionless time step becomes $\Delta t=1$.

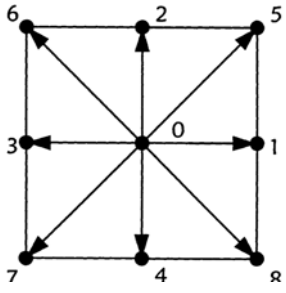

Fig. 1 The D2Q9 (2D with 9 velocity) lattice

The velocity vector $\boldsymbol{e}_i$ is determined in such way that the particle arrives at the other end of the link i after a unit time step. For instance, $\boldsymbol{e}_1=(1,0)$, $\boldsymbol{e}_5=(1,1)$, $\boldsymbol{e}_6=(-1,1)$, etc. The distribution functions contribute to the total density ρ, fluid momentum $\rho\boldsymbol{u}$ and density difference φ through the following equations:

$$\rho=\sum_{i=0}^{8}f_i^{eq}=\sum_{i=0}^{8}f_i \tag{3}$$

$$\varphi=\sum_{i=0}^{8}g_i^{eq}=\sum_{i=0}^{8}g_i \tag{4}$$

$$\rho\boldsymbol{u}=\sum_{i=0}^{8}f_i^{eq}\boldsymbol{e}_i=\sum_{i=0}^{8}f_i\boldsymbol{e}_i \tag{5}$$

In order to obtain the continuum equations pertinent to a binary fluid mixture, we need to derive the higher moments of $f_i^{eq}(\boldsymbol{r},t)$ and $g_i^{eq}(\boldsymbol{r},t)$ as follows.

$$\sum_{i=0}^{8}f_i^{eq}e_{i\alpha}e_{i\beta}=P_{\alpha\beta}+\rho u_\alpha u_\beta \tag{6}$$

$$\sum_{i=0}^{8}g_i^{eq}e_{i\alpha}=\varphi u_\alpha \tag{7}$$

$$\sum_{i=0}^{8}g_i^{eq}e_{i\alpha}e_{i\beta}=\Gamma\Delta\mu\delta_{\alpha\beta}+\varphi u_\alpha u_\beta \tag{8}$$

Here the subscript α and β denote the components along the x and y directions (respectively), $P_{\alpha\beta}$ is the pressure tensor, $\Delta\mu$ is the chemical potential difference between the two fluid components and Γ is a coefficient related to the mobility of the fluid. The formula of the local equilibrium distribution functions $f_i^{eq}(\boldsymbol{r},t)$ and $g_i^{eq}(\boldsymbol{r},t)$ which can be derived from these relations are listed in Appendix A for completeness (Orlandini et al., 1995; Swift et al., 1996; Xu et al., 2003 and 2004).

Following Xu et al. (2003), we introduce the free-energy function, defined as

$$F=\int dr\left[\frac{1}{3}\rho\ln\rho+\frac{a}{2}\varphi^2+\frac{b}{4}\varphi^4+\frac{\kappa}{2}(\nabla\varphi)^2\right] \tag{9}$$

This is used to implement the surface-tension

effect as well as to control the rate of the phase segregation. The first term in the integrand gives rise to a positive background pressure and does not affect the phase behavior. The other terms having φ are needed for the phase separation to take place. The parameter b is always positive, but a negative value must be chosen for a, so that it leads to the mixture's segregation (Xu et al., 2003). Further, we set $b=-a$ so that the equilibrium values for the order parameter become the predetermined ones ($\varphi=\pm 1$).

By performing the one-dimensional analysis it can be shown that the dimensionless surface tension is given by

$$\sigma=\frac{-2a}{3b}\sqrt{-2a\kappa} \tag{10}$$

and an interfacial width by

$$\xi=2\sqrt{\frac{2\kappa}{-a}} \tag{11}$$

The relation between the dimensional and non-dimensional surface tension parameters is elaborated in Appendix A. The chemical potential difference used in equations (A13) and (A17) in the Appendix is then given by

$$\Delta\mu=\frac{\delta F}{\delta\varphi}=a\varphi+b\varphi^3-\kappa\nabla^2\varphi \tag{12}$$

and the pressure tensor, $P_{\alpha\beta}$ appearing in Eqn. (6) takes the form

$$P_{\alpha\beta}=p_0\delta_{\alpha\beta}+\kappa\partial_\alpha\varphi\partial_\beta\varphi \tag{13}$$

where

$$p_0=\frac{1}{3}\rho+\frac{a}{2}\varphi^2+\frac{3b}{4}\varphi^4-\kappa\varphi\nabla^2\varphi-\frac{\kappa}{2}(\nabla\varphi)^2 \tag{14}$$

The dimensionless kinematic viscosity ν is given by

$$\nu=\frac{2\tau-1}{6} \tag{15}$$

Two types of the boundary conditions are applied in this simulation. At the inlet and on the solid walls, the bounce-back boundary condition is applied, whereas at the outlet the extrapolation schemes are used. On the solid walls of the channel, where the no-slip and impermeable restrictions are to be satisfied, the bounce-back boundary conditions are used. Bounce-back means that, when a particle distribution streams to a wall node, the particle distribution scatters back to the same node from which it came. For instance, when the boundary wall is horizontal and is located just at the mid position between the fluid and solid nodes as shown in Fig. 2, the distribution function at the fluid node along the link 4 after the collision process is $\tilde{f}_4(\boldsymbol{r}_f, t)$, and this is to be transmitted to the solid node after the streaming process. In the streaming process, the same solid node must in turn transmit the function $\tilde{f}_2(\boldsymbol{r}_s, t)$ to the fluid node. In this case, $\tilde{f}_2(\boldsymbol{r}_s, t)=\tilde{f}_4(\boldsymbol{r}_f, t)$ is set, so that the mass as well as the momentum should be in principle conserved. In general, this can be written as follows:

$$\tilde{f}_{\bar{\alpha}}(\boldsymbol{r}_s, t)=\tilde{f}_\alpha(\boldsymbol{r}_f, t) \tag{16}$$

where $\bar{\alpha}$ denotes the direction opposite to α.

The boundary conditions at the three inlets are also treated by using the bounce-back scheme. Parabolic profile is applied for all the inlet velocities. For instance, at the inlet shown in Fig. 3, we use the following formula.

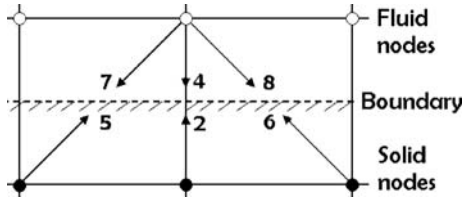

Fig. 2 Schematic for illustrating the bounce-back boundary condition

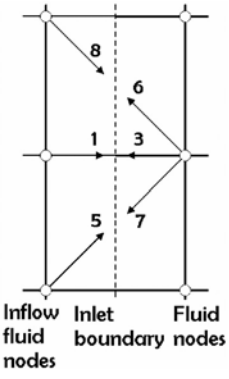

Fig. 3 Schematic for illustrating the inflow boundary condition

$$\tilde{f}_{\bar{\alpha}}(\boldsymbol{r}_{\text{in}}, t) = \tilde{f}_{\alpha}(\boldsymbol{r}_{\text{f}}, t) + 6 w_{\alpha} \rho_{\text{in}} \boldsymbol{e}_{\bar{\alpha}} \boldsymbol{u}_{\text{in}} \quad (17)$$

$$\tilde{g}_{\bar{\alpha}}(\boldsymbol{r}_{\text{in}}, t) = \tilde{g}_{\alpha}(\boldsymbol{r}_{\text{f}}, t) + 6 w_{\alpha} \rho_{\text{in}} \boldsymbol{e}_{\bar{\alpha}} \boldsymbol{u}_{\text{in}} \quad (18)$$

where w_{α} is the weighting factor (Yu et al., 2003; Qian, 2003) Here ρ_{in} is the density of the inlet fluid, which is taken to be unity.

At the outlet, the Neumann boundary condition is applied. At every link, the first-order extrapolation scheme for f is given by (Nourgaliev et al., 2003)

$$\tilde{f}_{\alpha}(\boldsymbol{r}_{\text{o}}, t) = \tilde{f}_{\alpha}(\boldsymbol{r}_{\text{f}}, t) \quad (19)$$

and the second-order extrapolation for g,

$$\tilde{g}_{\alpha}(\boldsymbol{r}_{\text{o}}, t) = 2\tilde{g}_{\alpha}(\boldsymbol{r}_{\text{f}}, t) - \tilde{g}_{\alpha}(\boldsymbol{r}_{\text{ff}}, t) \quad (20)$$

are used for this purpose (Yuan, 2005). Here the subscript ff denotes the node one more step upstream of the node f.

3. Model Description

In order to study the droplet dynamics of the binary fluid, a cross-junction channel is considered in the micro scale having three inlets and one outlet as shown in Fig. 4. A similar setup is employed by Kim et al.(2004), who conducted flow visualization experiment and reported the droplet generation process as well as the velocity measurement around the droplets. The width of the horizontal (main) channel is set as 200 μm and that of the vertical channel as 100 μm. The fluid component A is injected through the horizontal channel inlet with a parabolic profile with the maximum velocity U_{in}. The fluid component B is admitted from two vertical-channel inlets with the maximum velocity V_{in}. The ratio of the two velocity magnitudes, $V_{\text{in}}/U_{\text{in}}$ is fixed as 6. Since the flow rate of the fluid A is 6 times smaller than that of B, the droplet is expected to be composed of the A fluid only.

For the purpose of computational convenience, the channel is divided into three blocks as shown in Fig. 5. Uniform Cartesian grids are built within each block. The actual number of grids along each direction is also indicated in Fig. 5. Calculation is performed in each region separately. After that, data are exchanged with each other at

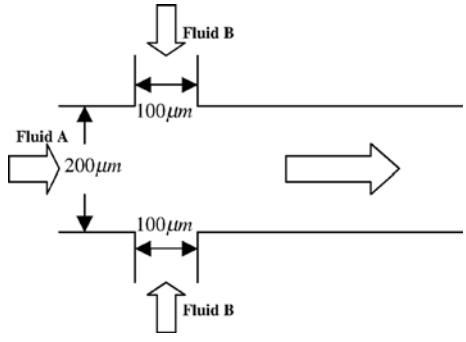

Fig. 4 Cross-junction microchannel model

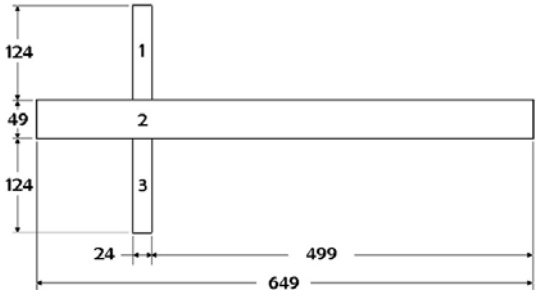

Fig. 5 Mesh setup of the cross-junction micro channel

the overlapped nodes which are necessary for the streaming step and for calculation of the derivatives.

The parameters involved in the present simulation are $a, b, \kappa, \Gamma, U_{\text{in}}, V_{\text{in}}$, and the channel geometry. Initially we set $-a = b = \kappa$ and change κ to control the surface tension. The inlet velocities at the centerline of each channel are fixed as $U_{\text{in}} = 0.014$ and $V_{\text{in}} = 0.084$.

The density of the two fluid components at the inlet are set as $\rho_a = \rho_b = 1.0$

4. Numerical Stability and Accuracy

After several test runs, it was found that the numerical scheme reveals a stability problem. The stability of the scheme depends on the values of τ. Γ and κ. Figures 6(a) to 6(c) show the stability chart each with one among these three parameters fixed. It can be seen from Fig. 6(a) that there is the upper limit of Γ (≈ 3.5) beyond which the scheme becomes unstable. The limit value is

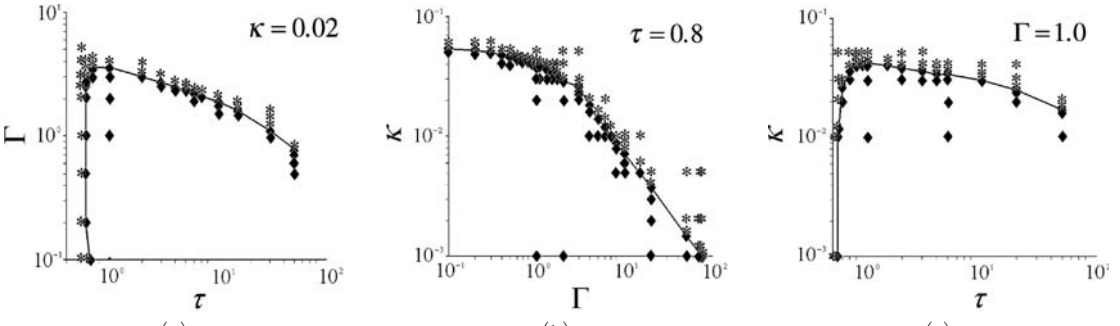

Fig. 6 Stability charts for the three parameter (τ, Γ, κ) combinations: (a) Γ vs τ at $\kappa=0.02$, (b) κ vs Γ at $\tau=0.8$ and (c) κ vs τ at $\Gamma=1.0$ (◆ Stable; ∗ Unstable)

slowly decreasing as τ is increased. It also shows that the scheme fails to produce the converged solutions at about $\tau<0.7$. Figure 6(b) implies that the upper limit of κ is continuously decreasing as Γ is increased. Figure 6(c) exhibits the weak dependence of the upper limit of κ on τ. All of these plots are useful in determining the parameter values for use in the actual numerical experiments.

The numerical accuracy of the solutions obtained by the developed code is also rigorously checked. The channel geometry (and so the number of grids in each dimension) is fixed as shown in Fig. 7. The value of n_y only needs to be changed for different number of grids.

The standard velocity field used in the accuracy analysis is the parabolic velocity profile (which is the exact solution for the case of the fully-developed simple channel flow). The numerical solution for the purpose of comparison is taken from the velocity profile at the cross section $x=7n_y$, where the flow is almost fully developed. The Reynolds number value is fixed as 1 and the same fluid is assumed to enter through all the three inlets for this test.

The error value is defined as

$$E=\sqrt{\sum_{j=1}^{n_y}(\tilde{u}_j-u_j)^2/n_y} \tag{21}$$

where $\tilde{u}_j$ is the normalized velocity value obtained numerically and u_j is the normalized exact solution;

$$u_j=1-\left[\frac{2j-(n_y+1)}{n_y}\right]^2 \tag{22}$$

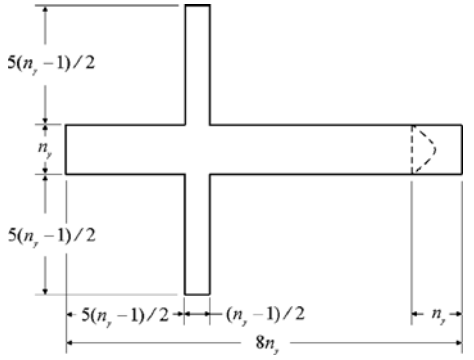

Fig. 7 Set-up of the channel geometry (and so the the grid system used in the study) on the numerical accuracy

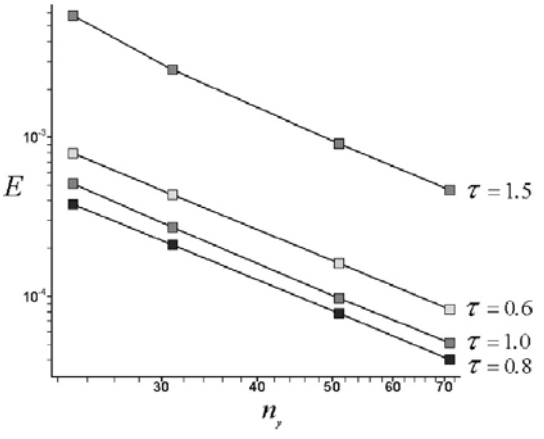

Fig. 8 Numerical accuracy of the present code

The numerical error E obtained in this way is plotted with four different n_y values (n_y=23, 31, 51 and 71), and under four different relaxation times (τ=0.6, 0.8, 1 and 1.5) as shown in Fig. 8.

From this figure it can be understood that the present numerical scheme assures the 2nd order accuracy.

5. Numerical Results

The numerical experiments were conducted with the same grid system and boundary conditions that are used for the stability test. The relationship $-a=b=\kappa$, $\tau_\rho=\tau_\varphi$ and the density value, $\rho_a=\rho_b=1.0$ are fixed in this simulation. The density difference, φ, is plotted to depict the droplet formation and its movement.

The initial condition for φ is given in Fig. 9. The area in grey indicates fluid A, and that in black fluid B. The standard parameter values, otherwise stated in the following analysis, are $\Gamma=0.3$, $-a=b=\kappa=0.04$, $\tau_\rho=\tau_\varphi=1.67$, $U_{in}=0.000652$, $V_{in}=6U_{in}=0.003912$. For this case, the value of Reynolds number is maintained as 0.58 and the time step (Δt) as unity. The maximum time limit, T is set as 2500, for convenience.

The processes of generation and separation of the droplets are shown in Fig. 10. It can be understood that, under this condition, fluid A is separated leading to a series of uniform array of droplets. The droplets move with surrounding fluid B without being mixed.

To investigate the methods to control the phenomenon of droplet formation in the cross-junction microchannel, a series of simulations with three different values of the mobility ($\Gamma=0.01$, 0.1 and 0.3) and two Reynolds number values ($Re=0.29$ and 0.58) are carried out. The numerical results obtained are shown in Fig. 11. With larger value of Γ, the droplet becomes more round in the shape (Fig. 11). At higher Reynolds number values, the droplet separation is expected to be more difficult. Accordingly, the droplets in the lower group of figures in Fig. 11 are smaller than those in the upper ones.

The present numerical results are compared with the experimental ones reported by Kim et al. (2004). In order to carry out this comparison, a number of attempts have been made for doing the numerical simulation with the same Reynolds number as used by them in their experiment. How-

Fig. 9 Initial distribution of φ in the cross-junction channel

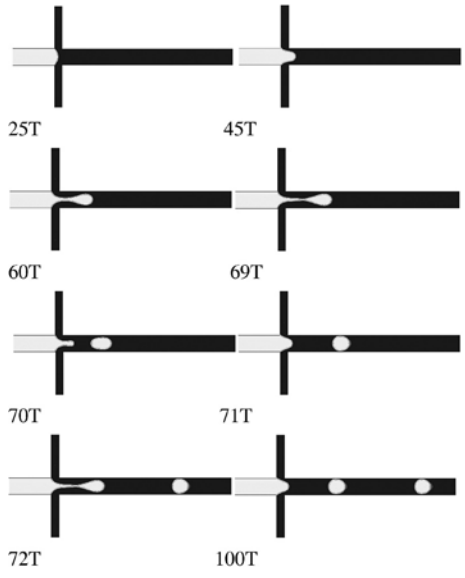

Fig. 10 Generation and motion of the droplets in the cross-junction channel (with the standard parameter values)

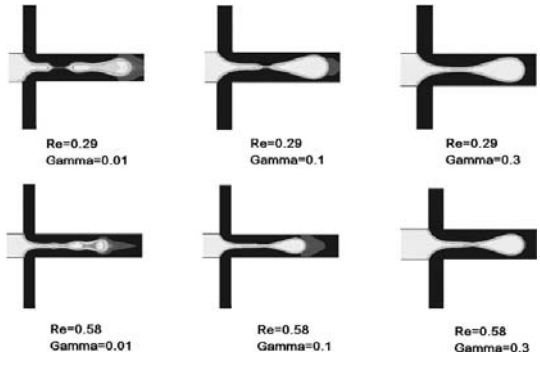

Fig. 11 Droplet formation phenomenon obtained by changing the value of Re and Γ (The other parameters follow the standard parameter set)

ever, it was not successful, due to the stability problem and the limited capability of the computer used. Hence, the velocity values are increased to shorten the computation time. For making the parameters close enough, $Re=0.29$ and $\Gamma=0.3$ are chosen for the calculations to compare with the experiment data of Kim et al.(2004). Figure 12 pictorially represents this comparison at different time instances. The process of droplet formation in the cross-junction area is clearly depicted in these pictures. Figure 12(a) shows the immediate state after a droplet is fully formed. Figures 12(b) to 13(d) show the following stages of droplet formation process. A more round shaped droplet is noticed in the experimental results and also the separation occurred more quickly in the experiment than in the numeric. The droplet obtained by the numerical simulation is not round enough and need longer distance for separation (Fig. 12(d)).

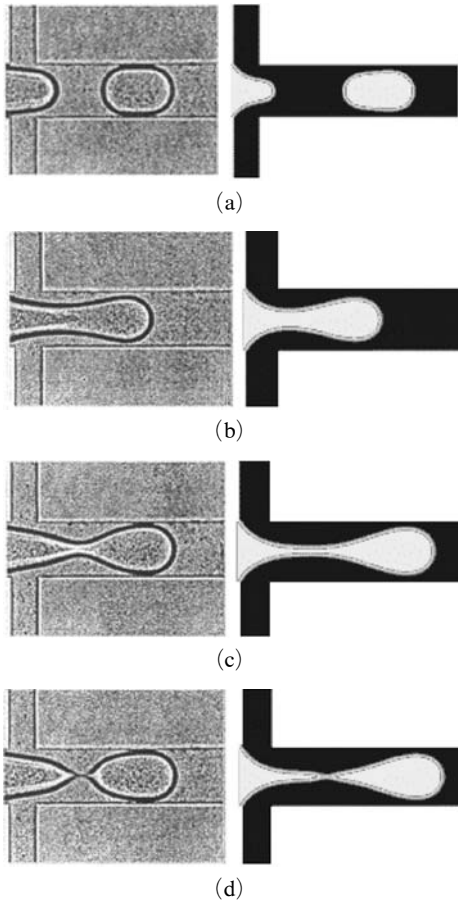

Fig. 12 Comparison of the present numerical results at $Re=0.29$ with the experimental results of Kim et al.(2004)

However, the qualitative nature of the result matches in both cases. The reasons for the quantitative disparity between the experimental and numerical results are elaborated in the following paragraph.

In the experiments conducted by Kim et al. (2004), water phase is injected from the horizontal inlet with the flow rate 0.9 [μl/min] and simultaneously the organic phase (oil) is injected from the vertical inlets with the flow rate 0.3 [μl/min]. The surface tension value of the oil is 26×10^{-3} [N/m] and for water phase it is 45×10^{-3} [N/m]; so the relative surface tension is 19×10^{-3} [N/m]. The dynamic viscosity is 24.4 [mm^2/sec] (at 19.7±0.3℃) for the organic phase and 10.7 [mm^2/sec] (at 23±2℃) for the water phase. The width of the horizontal part of the channel is 200 [μm] and the width of the vertical part is 100 [μm]. The height is 100 [μm] everywhere. With this data the Reynolds number value works out to be 0.029. In the numerical simulation we set the dimensionless parameters as $\tau_\rho=\tau_\varphi=1.67$, $-a=b=\kappa=0.04$, $U_{\text{in}}=0.000326$, $V_{\text{in}}=0.001956$ and $\Gamma=0.3$. These values correspond to the mean dynamic viscosity 18 [mm^2/sec] and the difference of surface tension 20×10^{-3} [N/m]. The Reynolds number value for the numerical analysis works out to be 0.29, which is incidentally 10 times that used for the experiments. This is done due to the reason that, the Reynolds number value is already very small and the computational time would be quite considerable for the numerical simulation at $Re=0.029$. On a good-quality personal computer with latest specifications, it will take about a month to get the converged results for the case of $Re=0.029$. Also it should be noted that the numerical results presented in Fig. 13 are obtained with the two-dimensional formulation. The basic reason for such difference between two and three-dimensional configuration may be explained in terms of the sectional view of the channel including the droplet.

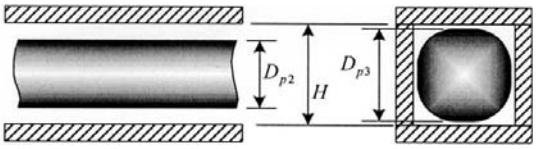

(a) 2-D (b) 3-D

Fig. 13 The cross-sectional view of the droplets in 2-D and 3-D cases

Figure 13 demonstrate the fundamental difference in the shape of the droplet in the sectional view. For the 2-D case, the droplet takes an infinite strip as shown in Fig. 13(a), while for the 3-D case it takes almost a circular shape. The fluid B flows through the passage between the channel wall and the droplet surface. The flow rate has been predetermined as the boundary conditions at the inlets. Now the average flow velocity through the passages will be given by the flow rate of fluid B divided by the cross sectional area. Thus, if the gap is large, the passage velocity become small, and vice versa. The passage velocity plays important role in the droplet motion, because it will determine the viscous shear force acting on the droplet. In fact, for the case of steady state, we expect a force balance between this shear force and the net pressure force arising from the pressure difference between the upstream and downstream side of the droplet ; that is the pressure difference exerts the forward motion while the shear force exerts resistive effect. We may therefore roughly say that the cross-sectional area should be in the same level for 2-D and 3-D cases. As can be seen from Fig. 13(b), the 3-D configuration has four corners, and, because of the round shape of the droplet, the gap between channel wall and the droplet surface must be larger as the corner is approached. Therefore we can understand why the droplet looks larger in 3-D than in 2-D when looked from side of the channel.

The main purpose of the present work is to compare our LBM results with experimental data and make sure that the present method is suitable for the simulation of droplet formation in cross-junction microchannel. By the reason explained above we are satisfied to have a slightly smaller droplet size for the 2-D case than the 3-D case. On the other hand it is straightforward to extend our 2-D code to the 3-D problem after deriving the corresponding equilibrium functions. The similarity of the results between experimental (Kim et al., 2004) and present numerical is indicative of the suitability of the free energy based LBM for droplet simulation in microchannels.

6. Conclusions

It has been shown by the present analysis that the free energy model of the LBM can be used for the simulation of the droplet motion in microchannels. At a certain parameter set, the droplets can be uniformly generated in the junction area of the two-dimensional cross-junction microchannel. But in the dimensionless simulation algorithm carried out presently, several parameters are involved and it is difficult to exercise control over them. Numerical experiments were also conducted in order to test the stability and accuracy, under the fixed boundary conditions. The region in which the parameters are stable during the simulation is determined. The accuracy of the present simulation is proved to be of second order. A dimensional transformation was then carried out in order to relate the numerical and experimental data. This may be useful for implementation with the other two algorithms of LBM as well.

Various Γ and Re values are tried with the cross-junction microchannel, in which the droplet formation was analyzed. The numerical results obtained indicate that, the shape of the droplet is remarkably changed with the change of the mobility value, Γ. When the value of Γ is larger, the shape of the droplet formed in the channel is more like an ellipse. The Reynolds number value also can influence the shape of the droplet. At higher Reynolds numbers, the droplets are smaller in size. These require further validation by experiments with cross-junction microchannels.

The numerical results obtained during the present study are found to be having qualitative similarity with the experimental results reported in literature. However, there are quantitative changes in both cases due to the different Re values and the multi-dimensional effect. The two-dimension-

al simulation carried out presently is quite important, as it proves the validity of LBM for predicting the phenomenon of droplet formation in cross-junction microchannel.

Acknowledgments

This work was supported from the National Research Laboratory Program of the Korea Science and Engineering Foundation. Appreciation should also be given to Professor S. Jayaraj for reading the first version of the manuscript.

References

Gunstensen, A. K., Rothman, D. H., Zaleski, A. and Zanetti, G., 1991, "Lattice Boltzmann Model of Immiscible Fluid," *Physical Review A*, Vol. 43, pp. 4320～4327.

Kim, K. C., Kim, J. M. and Yoon, S. Y., 2004, "Simultaneous Measurement of Internal and External Flow Fields around the Droplet Formation in a Microchannel," *4th KSV Conference*, Korea, pp. 80～83.

Nourgaliev, R. R., Dinh, T. N., Theofanous, T. G. and Joseph, D., 2003, "The Lattice Boltzmann Equation method : Theoretical Interpretation, Numerics and Implications," *Multiphase Flows*, Vol. 29, pp. 117～169.

Orlandini, E., Swift, M.R. and Yeomans, J. M., 1995, "A Lattice Boltzmann Model of Binary-Fluid Mixtures," *Europhysics Letters*, Vol. 32, No. 6, pp. 463～468.

Qian, D. Y., 2003, *Bubble Motion, Deformation and Breakup in Stirred Tanks*, Ph.D. Dissertation, Clarkson University, USA.

Shan, X. and Chen, H., 1993, "Lattice Boltzmann Model for Simulating Flows with Multiple Phases and Components," *Physical Review E*, Vol. 47, pp. 1815～1819.

Succi, S., 2001, *The Lattice Boltzmann Equation for fluid Dynamics and Beyond*, Clarendon Press, Oxford

Suh, Y. K. and Kang, S. M., 2006, "Assessment of Algorithms for the No-Slip Boundary Condition in the Lattice Boltzmann Method," (submitted)

Sukop, M. C. and Thorne, D. T., 2006, *Lattice Boltzmann Modeling*, Springer, The Netherlands

Swift, M. R., Orlandini, E., Osborn, W. R. and Yeomans, J. M., 1996, "Lattice Boltzmann Simulation of Liquid-Gas and Binary Fluid Systems," *Physical Review E*, Vol. 54, No. 5, pp. 5041～5052.

Xu, A., Gonnella, G. and Lamura, A., 2003, "Phase-Separating Binary Fluids Under oscillatory Shear," *Physical Review E*, Vol. 67, pp. 056105-1～056105-14.

Xu, A., Gonnella, G. and Lamura, A., 2004, "Phase Separation of Incompressible Binary Fluids with Lattice Boltzmann Methods," *Physical A*, Vol. 331, pp. 10～22.

Yu, D. Z., Mei, R. W., Luo, L. S. and Shyy, W., 2003, "Viscous Flow Computations with the Method of Lattice Boltzmann Equation," *Progress in Aerospace Sci.*, Vol. 39, pp. 329～367.

Yuan, P., 2005, *Thermal lattice Boltzmann two-phase flow model for fluid dynamics*, Ph.D. Dissertation , University of Pittsburgh, USA.

Appendix A

The local equilibrium distribution functions in the free energy model described in Section 2 can be expressed as an expansion at the second order in the velocity $\boldsymbol{u}$ as follows (e.g. Orlandini et al., 1995 ; Swift et al., 1996).

$$f_0^{eq}=A_0+C_0\boldsymbol{u}^2 \tag{A1}$$

$$f_i^{eq}=A_{\mathrm{I}}+B_{\mathrm{I}}\boldsymbol{u}_\alpha\boldsymbol{e}_{i\alpha}+C_{\mathrm{I}}\boldsymbol{u}^2+D_{\mathrm{I}}\boldsymbol{u}_\alpha\boldsymbol{u}_\beta\boldsymbol{e}_{i\alpha}\boldsymbol{e}_{i\beta}+G_{\mathrm{I},\alpha\beta}\boldsymbol{e}_{i\alpha}\boldsymbol{e}_{i\beta} \quad (i=1,2,3,4) \tag{A2}$$

$$f_i^{eq}=A_{\mathrm{II}}+B_{\mathrm{II}}\boldsymbol{u}_\alpha\boldsymbol{e}_{i\alpha}+C_{\mathrm{II}}\boldsymbol{u}^2+D_{\mathrm{II}}\boldsymbol{u}_\alpha\boldsymbol{u}_\beta\boldsymbol{e}_{i\alpha}\boldsymbol{e}_{i\beta}+G_{\mathrm{II},\alpha\beta}\boldsymbol{e}_{i\alpha}\boldsymbol{e}_{i\beta} \quad (i=5,6,7,8) \tag{A3}$$

$$g_0^{eq}=a_0+c_0\boldsymbol{u}^2 \tag{A4}$$

$$g_i^{eq}=a_{\mathrm{I}}+b_{\mathrm{I}}\boldsymbol{u}_\alpha\boldsymbol{e}_{i\alpha}+c_{\mathrm{I}}\boldsymbol{u}^2+d_{\mathrm{I}}\boldsymbol{u}_\alpha\boldsymbol{u}_\beta\boldsymbol{e}_{i\alpha}\boldsymbol{e}_{i\beta} \quad (i=1,2,3,4) \tag{A5}$$

$$g_i^{eq}=a_{\mathrm{II}}+b_{\mathrm{II}}\boldsymbol{u}_\alpha\boldsymbol{e}_{i\alpha}+c_{\mathrm{II}}\boldsymbol{u}^2+d_{\mathrm{II}}\boldsymbol{u}_\alpha\boldsymbol{u}_\beta\boldsymbol{e}_{i\alpha}\boldsymbol{e}_{i\beta} \quad (i=5,6,7,8) \tag{A6}$$

The parameters in the above equations can be obtained by solving the Eqns. (3) to (8) given in Section 2. A suitable choice of the coefficients in expansions is

$$A_0=n-20A_{\mathrm{II}} \tag{A7a}$$

$$A_{\mathrm{I}}=4A_{\mathrm{II}} \tag{A7b}$$

$$A_{\mathrm{II}}=\frac{P_{\alpha\beta}\delta_{\alpha\beta}}{24} \tag{A7c}$$

$$B_{\mathrm{I}}=4B_{\mathrm{II}} \tag{A8a}$$

$$B_{\mathrm{II}}=\frac{n}{12c^2} \tag{A8b}$$

$$C_0=\frac{2n}{3c^2} \tag{A9a}$$

$$C_{\mathrm{I}}=4C_{\mathrm{II}} \tag{A9b}$$

$$C_{\mathrm{II}}=-\frac{n}{24c^2} \tag{A9c}$$

$$D_{\mathrm{I}}=4D_{\mathrm{II}} \tag{A10a}$$

$$D_{\mathrm{II}}=\frac{n}{8c^4} \tag{A10b}$$

$$G_{\mathrm{I},\alpha\beta}=4G_{\mathrm{II},\alpha\beta} \tag{A11a}$$

$$G_{\mathrm{II}\alpha\beta}=\frac{P_{\alpha\beta}-\frac{1}{2}P_{\sigma\sigma}\delta_{\alpha\beta}}{8c^2} \tag{A11b}$$

$$G_{\mathrm{II},xx}=-G_{\mathrm{II},yy}=\frac{P_{xx}-P_{yy}}{16c^2} \tag{A12a}$$

$$G_{\mathrm{II},xy}=G_{\mathrm{II},yx}=\frac{P_{xy}}{8} \tag{A12b}$$

$$a_0=\varphi-20a_{\mathrm{II}} \tag{A13a}$$

$$a_{\mathrm{I}}=4a_{\mathrm{II}} \tag{A13b}$$

$$a_{\mathrm{II}}=\frac{\Gamma\Delta\mu\delta_{\alpha\beta}\delta_{\alpha\beta}}{24} \tag{A13c}$$

$$b_{\mathrm{I}}=4b_{\mathrm{II}} \tag{A14a}$$

$$b_{\mathrm{II}}=\frac{\varphi}{12c^2} \tag{A14b}$$

$$c_0=\frac{2\varphi}{3c^2} \tag{A15a}$$

$$c_1=4c_{\mathrm{II}} \tag{A15b}$$

$$c_{\mathrm{II}}=-\frac{\varphi}{24c^2} \tag{A15c}$$

$$d_I=4d_{II} \tag{A16a}$$

$$d_{II}=\frac{\varphi}{8c^4} \tag{A16b}$$

$$g_{\mathrm{I},\alpha\beta}=4g_{\mathrm{II},\alpha\beta}=0 \tag{A17a}$$

$$g_{\mathrm{II}}=\frac{\Gamma\Delta\mu\delta_{\alpha\beta}-\frac{1}{2}\Gamma\Delta\mu\delta_{\sigma\sigma}\delta_{\alpha\beta}}{8c^2}=0 \tag{A17b}$$

The derivatives are obtained by the central difference algorithm. OUther terms can be obtained as follows

$$P_{xx}=p_0+\kappa\partial_x\varphi\partial_x\varphi \tag{A18}$$

$$P_{yy}=p_0+\kappa\partial_y\varphi\partial_y\varphi \tag{A19}$$

$$P_{xy}=\kappa\partial_x\varphi\partial_y\varphi \tag{A20}$$

$$P_{\alpha\beta}\delta_{\alpha\beta}=P_{xx}+P_{yy} \tag{A21}$$

$$P_{\sigma\sigma}\delta_{\alpha\beta}=P_{xx}+P_{yy} \tag{A22}$$

The formula relating the dimensional and dimensionless parameters in Section 2 is described here. This should be useful to carry out corresponding experimental visualizations for the purpose of comparison. The parameters with the superscript * in this Appendix indicates the dimensional reference unit. The total density ρ plays a role of the background density and pressure. In the present study, every node is only occupied by a single fluid. Hence, $\rho_a=\rho_b$ is set in order to get a uniform background. Also, $\rho_a^*=\rho_b^*=\tilde{\rho}$ is used, where $\tilde{\rho}$ is a temporary value. The non-dimensional density difference φ can be defined as the actual density difference divided by the reference density. Hence φ can be treated as an order parameter.

$$\varphi=\frac{\rho_a^*-\rho_b^*}{\tilde{\rho}} \tag{A23}$$

From Eqns. (10), (11) and (14) in Sec. 2, the reference units can be set as follows.
Interface thickness

$$\xi^*=\sqrt{\kappa^*/a^*} \tag{A24}$$

Surface tension

$$\sigma^*=\frac{2\sqrt{2}}{3}\sqrt{\kappa^* a^*} \tag{A25}$$

Pressure

$$p_0^*=\frac{a^*}{2}\varphi^2+\frac{3b^*}{4}\varphi^4 -\kappa^*\varphi(\nabla_*^2\varphi)-\frac{\kappa^*}{2}(\nabla_*\varphi)^2 \tag{A26}$$

From Eqns. (A24) to (A26), it can be derived that a^* and b^* are having the unit $[\mathrm{N/m^2}]$ whereas κ^* is of unit $[\mathrm{N}]$. As a^* and b^* are in the same unit as that of stress, it can be scaled as follows:

$$(a^*, b^*)=(a, b)\,[\rho_0^*(c^*)^2] \tag{A27}$$

Similarly, κ^* is in the same unit as the force. Hence,

$$\kappa^*=\kappa[\rho_0^*(c^*)^2(\Delta x^*)^2] \tag{A28}$$

The reference unit of surface tension is

$$\sigma^*=\frac{2\sqrt{2}}{3}\sqrt{\kappa a}\,[\rho_0^*(c^*)^2\Delta x^*] \tag{A29}$$

The reference unit of the kinematic viscosity is

$$\nu_0^*=\Delta x^* c^* \tag{A30}$$

Accordingly, the velocity reference unit c^* is defined as

$$c^*=\Delta x^*/\Delta t^* \tag{A31}$$